Materialia 12 (2020) 100735

Contents lists available at ScienceDirect

Materialia

journal homepage: www.elsevier.com/locate/mtla

Full Length Article

Tailoring electrostatic surface potential and adsorption capacity of porous ceramics by silica-assisted sintering

Marieke M. Hoog Antink[a], Sascha Beutel[b], Kurosch Rezwan[a,d], Michael Maas[a,d,*]

[a] Advanced Ceramics, University of Bremen, Am Biologischen Garten 2, 28359 Bremen, Germany
[b] Institute for Technical Chemistry, Leibniz University Hannover, Callinstraße 5, 30167 Hannover, Germany
[d] MAPEX – Centre for Materials and Processes, University of Bremen, 28359 Bremen, Germany

ARTICLE INFO

Keywords:
Microstructure formation mechanism
Yttria-stabilized zirconia polycrystal
Liquid phase sintering
Electrochemical characterization
Structure-property relationship

ABSTRACT

In this study, we apply silica-assisted sintering to develop porous yttria stabilized zirconia (YSZ) ceramics with tailored electrostatic surface potential and adsorption capacity as a promising alternative to chemical functionalization. The porous bodies were formed by partial sintering at 1050 °C and were investigated regarding the influence of admixtures of silica particles on sintering behavior, microstructural evolution and the resulting mechanical and surface properties of the material, particularly the surface potential. With increasing silica concentration, the sintering mechanism was gradually changed from solid state to liquid phase sintering, due to the wetting of YSZ by liquid silica and a resulting inhibition of mass transport, particle growth and diffusion-induced densification. Most importantly, due to the silica layer development, the isoelectric point (IEP) of the YSZ/silica material surfaces was systematically shifted towards the IEP of silica from pH 9.4 to 1.2 resulting in a more pronounced negative surface potential at neutral pH. The relationship between surface IEP and silica concentration was mathematically described using the IEPs of the starting materials, the YSZ particle radius and the glass layer thickness. This estimation allows us to tailor the surface coverage of the YSZ matrix with silica as well as the resulting electrostatic surface potential. We further demonstrate how the applied processing route can be effectively used to develop ceramics with specified adsorption capacities for protein immobilization for use in filtration, bioprocessing or biomaterial applications.

1. Introduction

The surface charge of oxide ceramic materials [1–4] critically determines the material's performance in application areas such as filtration [2,5], biomaterials, biomedical devices [6,7] and catalyst supports [8,9]. Chemical functionalization, like silanization [9–11], is frequently used to modify surface charge and other characteristics of ceramic materials without affecting their bulk properties [12,13]. However, such strategies often require poorly scalable protocols, especially if a well-defined, ultrathin surface coating is desired and they can show a limited stability against hydrolysis, especially at extreme pH conditions or against decomposition at elevated temperatures [12–15]. As an alternative, inorganic amorphous sintering additives might be used to modify ceramic surfaces without the need for chemical post-functionalization to generate a resistant and well-defined glassy surface coating with tailored surface charge.

For oxidic materials in aqueous environments, the electrostatic potential of the material surface is based on the charges of amphoteric hydroxyl groups [1–4] which are present at the solid/water interface. With surface charge and the resulting electrostatic potential, other important material properties, such as adsorption and ion exchange behavior [4,16], the interfacial energy and contact angle [1,17] and even the reflection of light [1] can be modified. The zeta potential, which represents the potential difference between a stationary layer of adsorbed ions on a solid surface and a surrounding diffuse, mobile ion layer, serves as a reliable indicator for a material's surface charge [2,18] with the isoelectric point (IEP) representing the pH at which the overall surface potential is zero [2,18]. Crystallographic defect structures [19], the nature and concentration of the surrounding electrolyte and especially the solid's stoichiometry and phase composition [2,4,8] have a strong impact on the zeta potential.

Amongst oxidic ceramics, zirconia-based materials play an important role as structural material [20–22]. Their characteristically high fracture toughness [22–24] and high damage tolerance [22] is achieved by transformation toughening due to cationic doping with CaO, MgO, CeO_2 or Y_2O_3 [20,23,25–27]. The incorporation of dopants in zirconia-based materials illustrates the effect of the chemical composition on a material's surface charge: While the IEP of pure monoclinic zirconia is

* Corresponding author at: Advanced Ceramics, University of Bremen, Am Biologischen Garten 2, 28359 Bremen, Germany.
E-mail address: michael.maas@uni-bremen.de (M. Maas).

https://doi.org/10.1016/j.mtla.2020.100735
Received 24 March 2020; Accepted 8 May 2020
Available online 19 May 2020

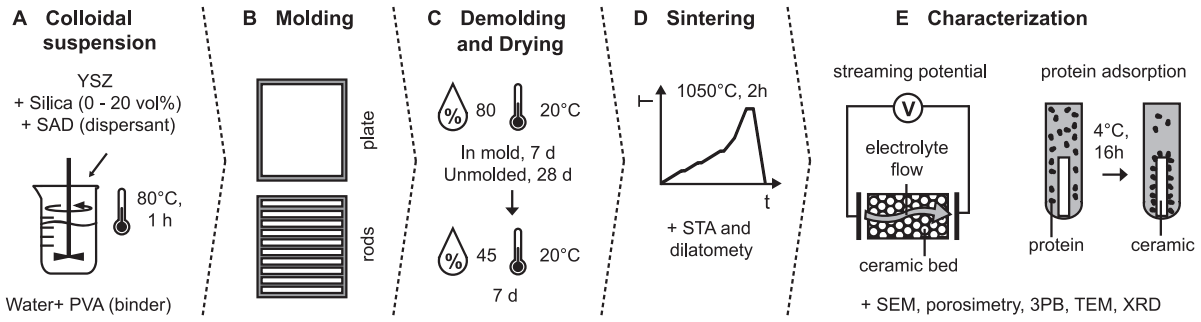

Fig. 1. Scheme of the processing and characterization process of YSZ/silica ceramics.

reported to be around pH 6.5 [1,28], it is shifted to pH 7.7–9.8 in yttria stabilized zirconia (3 mol%) [9,17,29]. To improve zirconia-based materials regarding their superior superplasticity [21,26,30–35] and other mechanical properties [23,26,31,36–38], their vulnerability to low temperature degradation [22,24,37–39] and ion conductivity [30], the effects of amorphous silica addition on the microstructure of densely sintered zirconia ceramics have been studied extensively. In this context, the effects of silica-assisted liquid phase sintering on densification [21,38,40–43], grain growth [21,26,34,35,41,44–46] and grain shape [21,24,26,31,35,41,44,45] and the locations of glass accumulation [23,24,30,33,35,37,43,44,47,48] have been investigated. However, regarding the relationship between the composition and microstructure of a mixed oxide material and its surface charge, no systematic evaluation has been conducted to the best of our knowledge.

Regarding membrane materials, Szymczyk et al. showed that silica impurities (9%) in Al_2O_3/TiO_2 ceramics significantly alter the electrokinetic properties by shifting the IEP to lower pH values [49]. In Al_2O_3:TiO_2:SiO_2 (7:3:1) membranes, Mullet et al. further concluded that the surface composition, and thus the surface electrochemical properties, differ from the bulk composition. Bowen and Mukhter evaluated ZrO_2:Al_2O_3:Y_2O_3 (8:5:1) membranes regarding their surface properties [50]. Although zirconia represented the higher weight fraction in the material, alumina – due to its smaller particle size – influenced the surface charge to a higher degree [50]. As a result of titania doping (5%) of alumina membranes, Zhang et al. observed a shift in the IEP towards the IEP of TiO_2 [2]. They showed how the surface charge modified the membrane flux and thus allowed to control membrane fouling [2].

In this study, we apply a silica-assisted sintering approach to prepare porous yttria stabilized zirconia ceramics with tailored surface properties. We investigate these materials primarily regarding their electrostatic surface potential and adsorption capacity. Ceramic dispersions with a silica content of up to 20 vol% are used to systematically study the material's microstructural evolution during sintering using dilatometry and high-resolution microscopy methods. This way, the role of the amorphous phase during the sintering process and its distribution in the microstructure can be evaluated. The resulting effect of the glassy phase on the material's mechanical properties, the zeta potential and adsorption capacities will be determined by three-point-bending (3 PB) tests, streaming potential experiments and adsorption of proteins as model colloids, respectively. For the first time, we will show how glassy sintering additives can be used to systematically tailor the electrostatic surface potential of a porous oxide ceramic matrix.

2. Experimental

2.1. Materials

All chemicals were used as received without further purification. Aerosil® 300 (average primary particle size = 7 nm, BET surface area 270–330 m^2/g, impurities as indicated by the manufacturer are presented in Table S2 of the Supplementary material) and vacuum grease (Schliff-Fett KaWeS, hardened carbohydrates, silicone-free) were purchased from Evonik, Germany, and Pöllath Labor Technologie, Germany, respectively. Bovine serum albumin (BSA, product no. A2153), HEPES (4-(2-Hydroxyethyl)piperazine-1-ethanesulfonic acid, product no. H3375), α-lactalbumin from bovine milk (α-LA, product no. L6010), lysozyme from chicken egg white (LYZ, product no. L6876), myoglobin from equine heart (MYO, product no. M1882), poly(vinyl alcohol) (PVA, Mw 31,000–50,000, 98–99% hydrolyzed, product No. 363138) and 5-sulfosalicylic acid dihydrate (SAD, product No. S2130) were acquired from Sigma Aldrich, Germany. The properties of the proteins bovine serum albumin, α-lactalbumin, lysozyme and myoglobin are summarized in Table S1 of the Supplementary material. Protein quantification was carried out with a Pierce® microplate BCA protein assay kit (reducing agent compatible, product no. 23252, Thermo Scientific™, Germany). Yttria stabilized zirconia powder TZ-3Y-E (YSZ, d_{50} = 40 nm, BET surface area = 16 ± 3 m^2/g, impurities as indicated by the manufacturer are presented in Table S2 of the Supplementary material) was obtained from Tosoh, Japan. Potassium chloride (KCl, product no. 26764) was purchased from VWR International GmbH, Germany. Ammonia (25%, product No. 1133.2500, VWR International GmbH, Germany), hydrochloric acid (HCl, 1 M, product no. 109057, Merck KGaA, Germany), potassium hydroxide solution (KOH, 1 M, product no. 35113, Honeywell Inc., USA), distilled water and double-deionized water (Millipore water, resistivity > 18 MΩ cm, SynergyUltra Water System Millipore Corp., USA) were used for the preparation of dispersions and solutions.

2.2. Methods

2.2.1. Fabrication of porous YSZ/silica monoliths

The preparation of YSZ/silica samples is summarized in Fig. 1(A–D). For the production of ceramic suspensions (Fig. 1(A)), 10 g of PVA were dissolved in 39 g of distilled water under 30 min of magnetic stirring at a temperature of 80 °C to yield a polymer concentration of 0.26 g/mL. The solution pH was adjusted to 9 using 1 mL of ammonia. Depending on the envisioned silica content (0, 0.1, 1, 5, 10, 20 vol%), ceramic powder mixtures of YSZ and silica with a total volume of 11.16 mL were prepared and $4.4689 \cdot 10^{-4}$ g/m^2 of SAD were added. The powder mixture was slowly added to the PVA solution under stirring and mixing was continued for 1 h using a Dispermat LC (VMA-GETZMANN GmbH, Germany). The resulting ceramic paste was directly filled into greased metallic molds (58 × 4 × 77 mm^3, Fig. 1(B)), which were covered by a PTFE layer at the top and bottom. For the preparation of rod-shaped bending samples, metallic insets were placed inside the molds to cast the suspension into geometries of 3 × 4 × 50 mm^3. All samples were firstly dried inside their molds for 1 week at 80% relative humidity (RH) and 20 °C, then demolded and placed on a polymeric foam and dried for another 4 weeks under the same environmental conditions.

Finally, the samples were exposed to 45% RH and 20 °C for 1 week. Prior to thermal treatment, the surfaces of the bending samples were manually ground down to 30 µm. Both sample types were debindered and sintered based on STA results (see Figs. S2 and S3) in one process in a LHT 08/17 oven (Nabertherm GmbH, Germany). First the unsintered bodies were heated with a rate of 0.5 K/min up to 650 °C and dwelling times of 1 h at 200, 310 and 470 °C and subsequently the temperature was increased up to the maximum sintering temperature of 1050 °C with 1 K/min and a holding time of 2 h. The nominal cooling rate was 5 K/min. For the dilatometric measurements, unsintered bending samples were shortened to a length of 10 mm. In contrast to the regular sintering process, these samples were heated up to 650 °C only.

2.2.2. Characterization of starting materials and porous YSZ/silica materials

Both ceramic powders and sintered porous YSZ/silica bodies were analyzed concerning their size or geometry, specific surface area, their behavior under high temperature treatment and their pH-dependent zeta potential. The monolithic samples were additionally characterized regarding their drying and sintering shrinkage, microstructure, porous properties, phase composition and bending strength.

The geometry of the oxide particles and the microstructure of sintered porous bodies was visualized by scanning electron microscopy (SEM, Supra 40-Carl Zeiss, Germany) and transmission electron microscopy (TEM). For the imaging of the silica powder Aerosil 300, a TEM-EM 900 was used (Carl Zeiss, Germany). Transparent slices of sintered, monolithic YSZ/silica samples with 0, 1 and 20 vol% silica were prepared for TEM measurements using a focused ion beam (FIB) lift-out technique on a FEI Nova 200 FIB. TEM investigations including HR-TEM, EDX and EDX line scans were performed with a TITAN 80/300 TEM/STEM microscope.

The particle size of the YSZ powder and the sintered microstructure was estimated based on SEM images and DIN EN 623-3 [51] using the linear intercept method. Per sample type, 3 SEM images and at least 500 particles were evaluated. The specific surface area of ceramic powders and monoliths was quantified by volumetric N_2 gas adsorption experiments with a BELSORP-mini (BEL Japan, Inc., Japan) apparatus followed by BET (Brunauer–Emmett–Teller) analysis. Prior to N_2 adsorption, the samples were treated at 120 °C for at least 3 h under vacuum (< 2 mbar) and subsequently exposed to an argon atmosphere at room temperature for 30 min. Thermogravimetric (TG) and differential thermal analysis (DTA) of all starting materials (including PVA and SAD) and unsintered samples was performed using a simultaneous thermal analyzer (STA 503, Bähr Thermoanalyse GmbH, Germany) to investigate the materials' response to high temperature treatment. Organic materials were heated up to up to a maximum temperature of 600 °C, the ceramic powders and unsintered samples up to 1400 °C, at a heating of 5 K/min. The dynamic light scattering (DLS) technique was used to determine the particle size of the YSZ and silica powders in Millipore water. The parameters of the DLS experiments are described in the Supplementary material S1.

The debindering and drying shrinkage of the YSZ/silica materials was evaluated by measurement of their sample geometry using a caliper. With a TMA 801S dilatometer (Bähr Thermoanalyse GmbH, Germany) the densification process of the ceramic samples was investigated regarding the differential change in sample length and the relative sintering shrinkage. The dilatometric analysis was performed using a heating rate of 2 K/min up to 1050 °C and a cooling rate of 5 K/min. The porosities and pore window size distribution of porous ceramic samples was investigated with a combination of two Hg porosimeters (Mercury Porosimeter Pascal 140 and 440, Porotec GmbH, Germany). Powder X-ray diffraction (XRD) was applied to investigate the phase composition of sintered, ground samples. The experimental parameters for XRD analysis are described in the Supplementary material S4. The bending strength (σ_f) of YSZ/silica samples was determined with the help of 3-point-bending tests (3 PB) according to DIN EN 843-1 [52]. The bending bars were tested with a Zwick/Roell Z005 static materials testing machine (ZwickRoell GmbH & Co. KG, Germany) on a 3 PB set-up with a support span of 30 mm at 45% RH and 21 °C. For each sample composition at least 30 samples were tested with a testing speed of 1 mm/min and a preload of 2 N. The bending strength was calculated using $\sigma_f = 3Fl/2bh^2$, where F is the maximum loading force in N, l is the support span (= 30 mm), b is the sample width (mm) and h is the height of the sample (mm). The data sets were analyzed using Weibull statistics to determine the characteristic strength σ_0 of the YSZ/silica materials and the Weibull modulus m.

Both ceramic powders and sintered YSZ/silica samples were characterized regarding their pH-dependent zeta potential. The colloidal vibration current and the dynamic light scattering technique were used to determine the zeta potential and the IEP of YSZ and silica particles, respectively. The experimental parameters of these experiments are described in the Supplementary material S1. The zeta potential of porous YSZ/silica ceramics was quantified in streaming potential measurements (Fig. 1(E)) using a SURPASS 2 electrokinetic analyzer (Anton Paar GmbH, Germany). Prior to the measurement, the plate-shaped samples were crushed and sieved to retain pieces between 90 µm and 1.12 mm. Approximately 0.6 g of this material was filled and densified inside a cylindrical measurement cell. The cell was incubated in Millipore water under sonication for at least 15 min. Streaming potential measurements were performed at 20 °C using 10 mM KCl as electrolyte, a target pressure of 100 mbar (0.01 MPa) and a rinsing time of at least 300 s per pH step. The pH titration was carried out starting from the natural pH of the solution (ca. pH 5.8) to pH 10 using 0.5 M HCl. Subsequently, the sample was rinsed with neutral electrolyte solution and the titration was continued towards the acidic range with 0.5 M KOH to at least pH 4 or until the IEP was encountered. The IEP was derived by linear interpolation between the two zeta potential values closest to a zeta potential of 0.

N_2 gas adsorption experiments, STA, SEM, TEM and DLS measurements as well as the determination of the drying shrinkage, dilatometric, porosimetry and streaming potential analysis were performed with $n \geq 3$.

2.2.3. Protein adsorption experiments

The effect of the ceramics' composition on the interaction of the surface with proteins in solution was investigated in protein adsorption experiments similar to Pasche et al. [53] (Fig. 1(E)). For this purpose, four different proteins (BSA, α-LA, LYZ and MYO) were individually dissolved in 10 mM HEPES buffer at pH 7 to yield concentrations of 0.5 mg/mL in Millipore water. α-LA, LYZ and MYO are characterized by a similar size and structure (14,200–17,800 g/mol, globular shape), but are characterized by significantly different IEPs of pH 4.3, 11.1 and 7.0, respectively (Table S1) [53,54]. BSA is a well-characterized standard protein, which served as reference material. It is characterized by a larger size than the other proteins (66,500 g/mol) but an IEP similar to α-LA (pH 4.7–4.8, Table S1) [10,55]. For the adsorption experiments, YSZ/silica bending samples with a length of 20 mm were weighed, washed in Millipore water, autoclaved (Systec™ VX-100, Systec, Germany) at 121 °C in steam atmosphere of 2 bar (0.2 MPa) pressure and dried at 70 °C for 24 h. The rods were individually placed in 2 mL reaction tubes and 1.75 mL of the respective protein solution were added. The ceramic samples were incubated for 16 h at 4 °C under shaking (150 rpm). Protein quantification was carried out photometrically by probing the supernatant with a BCA assay kit. The manufacturer's standard procedure for quantification of protein concentrations in microplates was applied. The absorbance values of three supernatant samples per YSZ/silica ceramic were measured at a wavelength of 562 nm with a Multiskan GO photometer (Thermo Scientific, Germany). The BSA, α-LA, LYZ and MYO protein concentrations in HEPES buffer were calculated based on individual reference curves. All adsorption experiments were performed in triplicates.

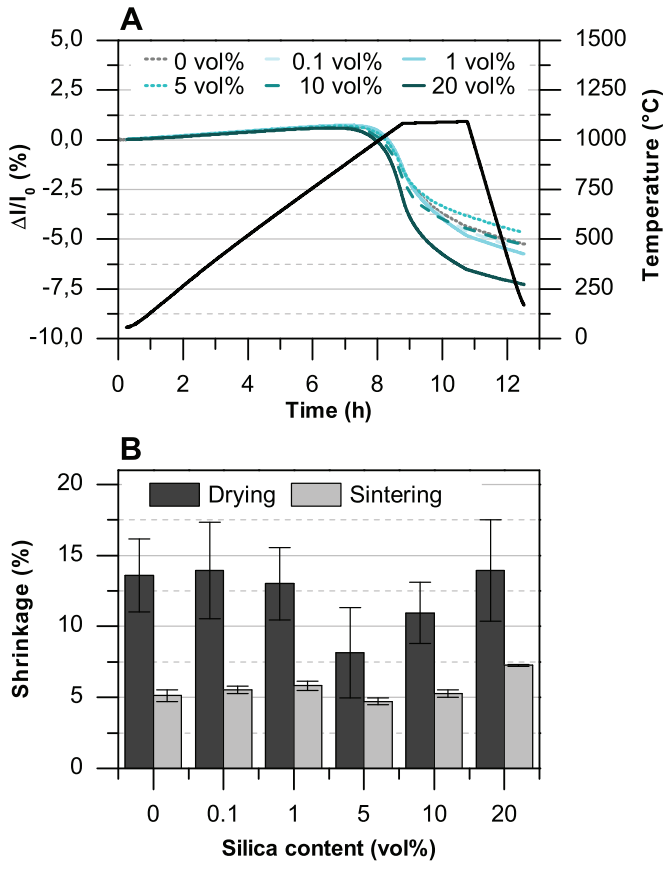

Fig. 2. Densification behavior of yttria stabilized zirconia (YSZ)/silica oxide samples with varying silica content. (A) Relative change in sample length (%) over time as determined by dilatometry. The corresponding temperature program is indicated in black (right hand *y* axis). (B) Mean drying and sintering shrinkage against the silica content of YSZ/silica samples as determined by manual geometric and dilatometric measurements, respectively. Error bars indicate the standard deviations between at least 3 measurements. The graphs in A and B are representative curves from triplicate measurements.

3. Results

3.1. Densification behavior of YSZ/silica samples

To analyze the effect of silica addition on the powder packing during the drying process of the YSZ/silica samples and on their sintering behavior, the densification during drying and sintering was monitored. Samples with varying silica content were investigated both by manual measurements of the sample geometry after drying and by dilatometric analysis of debindered samples during sintering. The results are shown in Fig. 2 and Table 1. Fig. 2 features representative curves from triplicate measurements. A summary of all dilatometric analysis results can be found in the Supplementary material in Figs. S4 and S5. Images of dried and sintered bending samples are shown in Fig. S10 of the Supplementary material.

During drying, the samples shrank by 8.1 ± 3.2 to 13.9 ± 3.6% with respect to the mold geometry (Fig. 2(C)). Due to the standard deviations, no significant differences between the samples regarding the drying shrinkage were found, but samples with a silica content of 5 and 10 vol% exhibited the smallest drying shrinkage values of 8.1 ± 3.2 and 10.9 ± 2.2%. To avoid warping and cracking of the samples, a controlled drying process (42 d) was chosen. For the application in an industrial manufacturing process, the drying period would have to be drastically reduced, e.g. by changing to an organic solvent for the preparation of the ceramic dispersion.

Debindering of the YSZ/silica samples was accompanied by a mean shrinkage of 0.5 ± 0.2% with respect to the dried samples (individual results are shown in Table S4 of the Supplementary information). As can be seen in Fig. 2(A), during temperature increase, all debindered YSZ/silica samples showed a thermal expansion up to a temperature of around 875 °C. After approximately 7 h and at a temperature of higher than 875 °C, a decrease in sample length was recorded. This is in agreement with the shrinkage rates (μm/min) of the samples, which remained constant up to ca. 875 °C and from this point on increased considerably in absolute value (Fig. S5). Both the samples with 10 and 20 vol% of silica showed increased shrinkage rates compared to samples with a lesser concentration of silica.

Compared to the size of the unsintered bodies, YSZ/silica samples exhibited a sintering shrinkage between 4.7 ± 0.2 for samples with 5 vol% of silica and 7.3 ± 0.2% for samples with 20 vol% silica (Fig. 2). Similar as during drying, the samples with 5 vol% silica showed the smallest sintering shrinkage, only now – with exception of the YSZ/0 vol% silica sample – this difference was significant. The YSZ/20 vol% silica samples on the other hand were characterized by the significantly highest sintering shrinkage.

3.2. Microstructure of porous YSZ/silica ceramics

To study the structural evolution in the silica-assisted sintering process, the effect of silica addition on the porous properties, specific surface area and other structural parameters of YSZ/silica ceramics was evaluated using mercury intrusion porosimetry, nitrogen adsorption experiments as well as electron microscopy methods. The size and shape of the ceramic powder materials and the microstructure of sintered oxide materials are depicted in Figs. 3 and 4. While the SEM images in Fig. 3(C)–(H) offer a more representative overview of the microstructure of all YSZ/silica sample types (0, 0.1, 1, 5, 10, 20 vol%)

Table 1
Properties of yttria stabilized zirconia/silica ceramics with varying silica content (vol%). SEM = scanning electron microscopy, LIM = linear intercept method, BET = Brunauer Emmett Teller analysis, 3 PB = 3-point-bending test.

Property	Technique	Silica content (vol%)					
		0	0.1	1	5	10	20
Shrinkage$_{Dry}$ (%)	Caliper	13.6 ± 2.6	13.9 ± 3.4	13.0 ± 2.6	8.1 ± 3.2	10.9 ± 2.2	13.9 ± 3.6
Shrinkage$_{Sint}$ (%)	Dilatometry	5.1 ± 0.4	5.5 ± 0.3	5.8 ± 0.3	4.7 ± 0.2	5.3 ± 0.3	7.3 ± 0.1
Density (g/cm^3)	Calculated	6.1	6.0	6.0	5.9	5.7	5.3
Particle size (nm)	SEM + LIM	76.8 ± 4.4	77.9 ± 1.0	69.1 ± 1.1	64.4 ± 1.0	62.2 ± 5.4	59.6 ± 1.0
Specific surface area (m^2/g)	N_2 adsorption + BET	7.2 ± 0.4	7.0 ± 0.5	9.0 ± 0.5	10.8 ± 1.0	11.5 ± 0.1	11.7 ± 0.1
Open porosity (%)	Hg porosimetry	51.2 ± 2.2	52.7 ± 0.8	53.3 ± 1.1	55.1 ± 1.1	53.1 ± 0.1	50.7 ± 0.2
Closed porosity (%)		0.7 ± 0.6	1.0 ± 0.4	1.3 ± 0.6	3.1 ± 3.1	1.4 ± 0.5	0.9 ± 0.2
Pore window size mode (nm)		93.0 ± 0.3	90.1 ± 5.6	81.2 ± 5.7	83.8 ± 7.7	75.4 ± 0.4	71.7 ± 2.3
Bending strength (MPa)	3PB	42.8	40.3	29.2	22.7	25.1	33.3
Weibull modulus		4.6	7.5	5.3	6.4	6.6	6.1
Isoelectric point (pH *units*)	Streaming potential	9.4 ± 0.3	8.5 ± 0.3	4.7 ± 0.1	2.7 ± 0.2	1.5 ± 0.3	< 1.2 ± 0.1

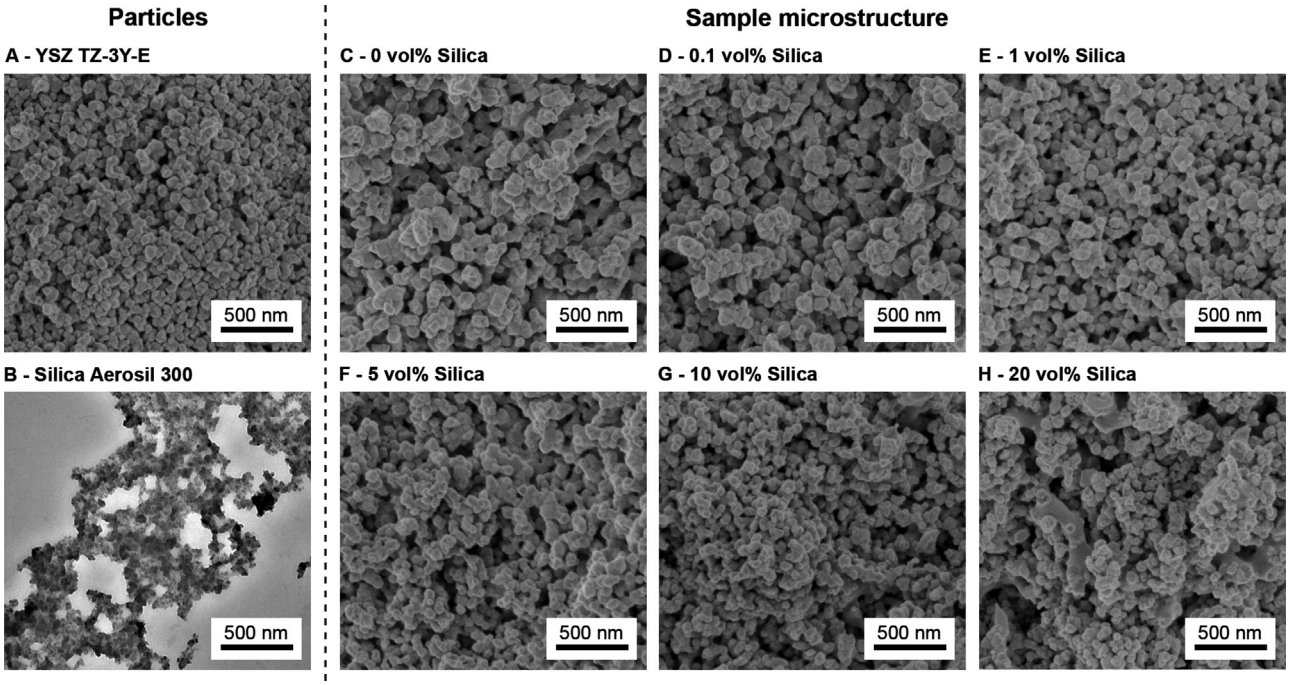

Fig. 3. Electron microscopic images of powder particles (A/B) and porous YSZ/silica ceramics with varying silica content (C–H). Images A and C–H were recorded using scanning electron microcopy, image B using transmission electron microscopy.

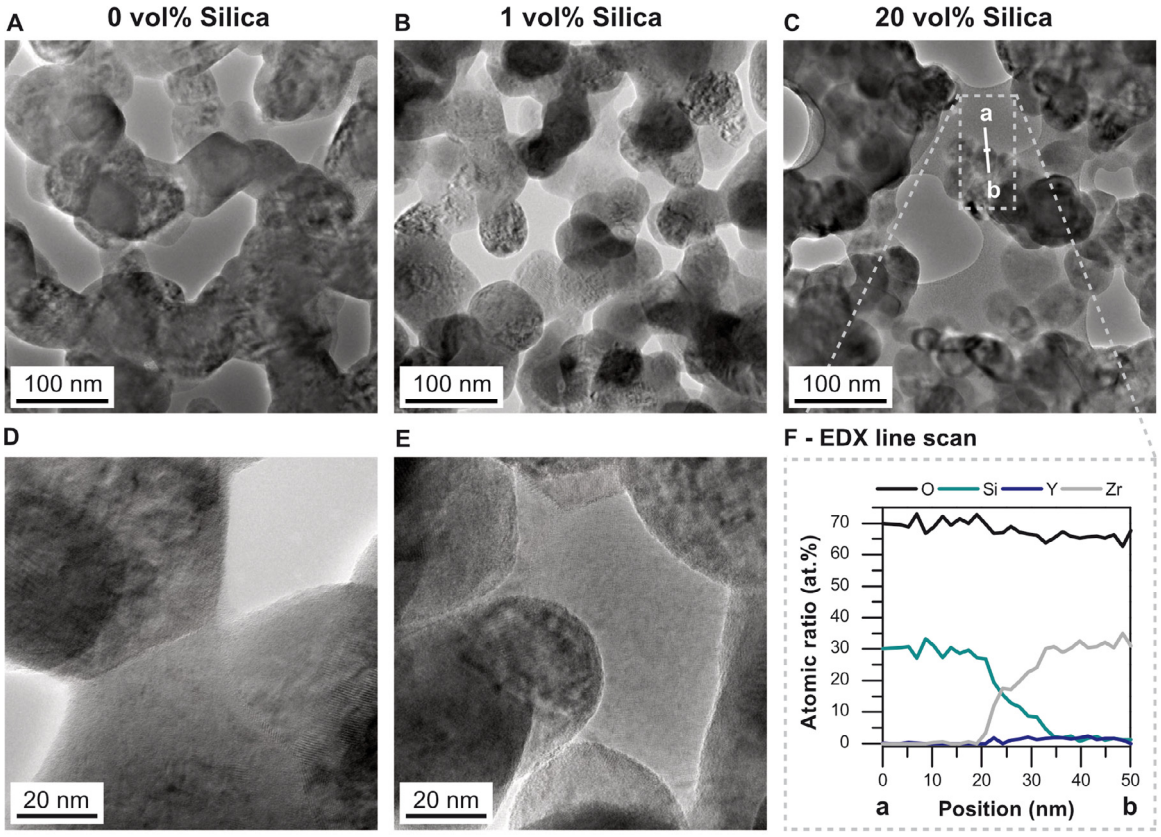

Fig. 4. TEM (A–C) and HR-TEM (D/E) image of porous YSZ/silica ceramics with varying silica content: 0 vol% silica (A/D), 1 vol% silica (B/E) and 20 vol% (C). F represents the results of an EDX line scan within the YSZ/20 vol% silica sample (C).

and thus useful in sampling a large number of particles regarding particle size, Fig. 4 presents high resolution TEM images of selected sample types (0, 1 and 20 vol%) to evaluate grain shape and particle boundaries in detail. Larger size SEM images of the microstructures can be found in Fig. S11 of the Supplementary information.

As can be seen in Fig. 3(A) and (B) and as suggested by the product information by the manufacturer, the particle size of silica is distinctly smaller than the particle size of the YSZ powder (7 vs. 40 nm). After the sintering process, single silica particles were not present in the microstructure, but next to YSZ particles, amorphous phases could be observed in silica containing samples, especially in the YSZ/20 vol% silica sample (Fig. 3(H), Fig. 4(C)). EDX measurements (Fig. 4(F)) in high-silica samples showed, that the amorphous phases were composed of SiO_2 only. On YSZ/1 vol% silica samples (Fig. 4(E)), some of the particle surfaces seem to be coated by a very thin amorphous layer, but the composition of those layers could not be unequivocally identified due to the scarcity of the material. After sintering, linear intercept measurements on SEM images of the microstructure of all YSZ/silica sample types indicated YSZ particle, which were enlarged by 5% to 34% compared to the initial particle size of 56.6 ± 3.1 nm of the YSZ starting powder (Table 1,Fig. 3,Fig. 4(A), Fig. 5(B)). With an increasing silica concentration in the sintered ceramic materials, this effect was however less pronounced: While YSZ/0 vol% silica samples featured a particle size of 76.8 ± 4.4 nm (34% increase), YSZ/20 vol% silica samples were characterized by a mean particle size of 59.6 ± 1.0 nm (5% increase). With a higher silica content, particles exhibited a more rounded shape (Fig. 4(A–E), Fig. 5(B)). At the same time, the specific surface area (SSA) of the samples slightly increased from 7.2 ± 4.4 (0 vol% silica) to 11.7 ± 0.1 m^2/g (20 vol% silica). But even for the sample with the highest silica concentration, the specific surface area remained significantly lower than the SSA of the YSZ powder material (14.8 ± 0.1 m^2/g, Table 1,Fig. 5(B)). Hg porosimetric analyses revealed that along with the mean particle size, the mean pore window size mode of the ceramic samples shifted towards lower values with increasing silica content (Table 1,Fig. 5(B)). Representative pore window size distributions of the YSZ/silica samples (Fig. 5(A)) illustrate a shift from 93.0 ± 0.3 nm (0 vol% silica) to 71.7 ± 2.3 nm (20 vol% silica). The overall porosity of the YSZ/silica samples varied only slightly in the range between 50.6 ± 0.2 and 55.1 ± 0.2% (Table 1,Fig. 5(B)). It increased with a silica addition up to 5 vol% from 51.2 ± 0.2 to a maximum of 55.1 ± 0.2% and decreased with a silica concentration > 5 vol% to 50.6 ± 0.2% in YSZ/20 vol% silica samples. The increase in overall porosity was mainly caused by an increase in the volume of closed pores. Silica-free and YSZ/20 vol% silica samples are characterized by a closed porosity of 0.7 ± 0.6% and 0.9 ± 0.2%, respectively, while the maximum volume of closed pores is reached at 3.1 ± 3.1% in samples with a silica content of 5 vol% (Table 1). A summary of the pore window size distributions of all sample replicates is given in Fig. S6 in the Supplementary material.

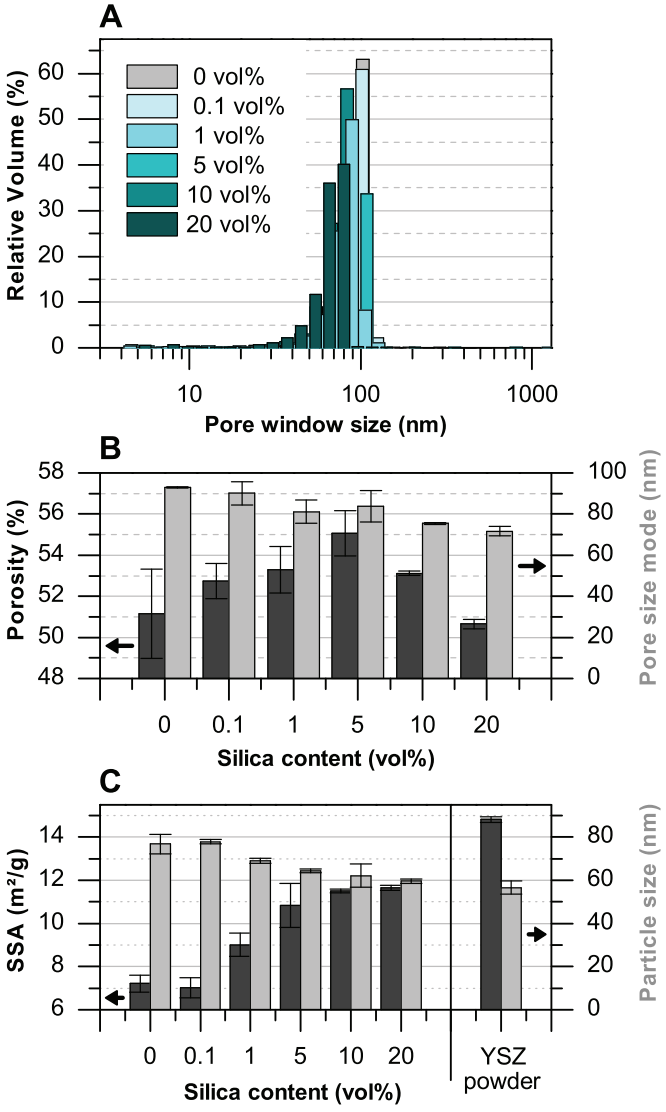

Fig. 5. (A) Representative pore window size distributions of YSZ/silica ceramics with varying silica content (vol%). (B) Mean porosity (%, dark grey) and pore window size (nm, light grey) of YSZ/silica samples with different silica content (vol%). (C) Mean specific surface area (SSA, m^2/g, dark grey) and particle size (nm, light grey) of porous YSZ/silica samples differentiated by silica content (vol%) and compared to the properties of unsintered YSZ powder. Error bars indicate the standard deviation between triplicates.

3.3. Strength of porous YSZ/silica materials

To evaluate the effect of microstructural differences between samples with varying amounts of silica on the bending strength (σ_f) of porous YSZ/silica ceramics, 3 PB tests were conducted. The results of these tests are summarized in Table 1 and Fig. S8. The characteristic strength of the samples varied between 42.8 MPa (0 vol% silica) and 22.7 MPa (5 vol% silica). While the addition of 0.1 vol% of silica to pure YSZ samples lowered the characteristic strength only slightly to 40.3 MPa, σ_f was more significantly reduced in samples with a silica concentration of 1 and 5 vol% (29.2 MPa/22.7 MPa). Compared to the strength minimum in YSZ/5 vol% silica samples, a further increase in silica content to 10 or 20 vol% resulted in higher characteristic strength values of 25.1 and 33.3 MPa, respectively. The strength distributions of each YSZ/silica sample type are characterized by the Weibull modulus (Table 1, Fig. S8), which indicates the width of the distribution. The smaller its value, the broader is the distribution of σ_f. The determined Weibull moduli lay within a narrow range between 4.6 (YSZ/0 vol% silica) and 7.5 for (YSZ/0.1 vol% silica).

3.4. Surface properties of YSZ/silica ceramics and interactions with proteins

Finally, the influence of silica concentration on the electrostatic surface potential and adsorption capacity of the YSZ/silica ceramics was systematically evaluated by streaming potential and protein adsorption experiments. The zeta potential as a function of pH and the mean isoelectric points (IEP) were both derived from the streaming potential experiments. Representative streaming potential curves of YSZ/silica ceramics with varying silica content are depicted in Fig. 6(A). Additionally a summary of all streaming potential measurements is given in Fig. S9 of the Supplementary material. The zeta potential of the ceramic materials ranged between 40 mV and –30 mV and decreased with increasing pH. The IEP, i.e. the pH value at which the zeta potential

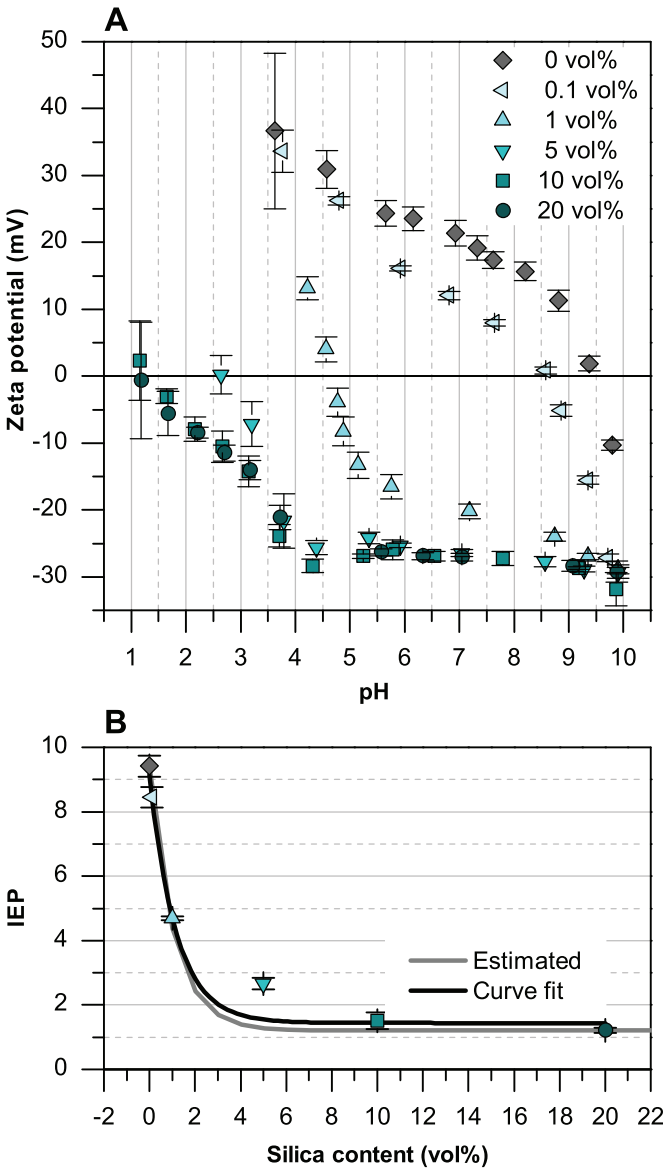

Fig. 6. (A) Representative streaming potential curves of porous yttria stabilized zirconia (YSZ)/silica ceramics with varying silica content (vol%). Error bars indicate the standard deviation between 4 individual measurements during one titration experiment on a single sample. (B) Isoelectric points of YSZ/silica ceramics against silica content (vol%). The gray and black graphs represent estimated and fitted exponential decay functions. The error bars indicate the standard deviation between 3 individual titration experiments.

equals 0 mV, was derived from linear interpolation of the datapoints. The IEP values started from pH 9.4 ± 0.3 (YSZ/0 vol% silica) and decreased to pH 1.2 ± 0.1 (YSZ/20 vol% silica) with increasing silica content. The zeta potential curves of YSZ/10 vol% and YSZ/20 vol% silica samples were very similar. The mean IEPs of YSZ/silica samples with increasing silica concentration are plotted in Fig. 6(B) and given in Table 1. The sample IEP was strongly affected by silica additions > 0.1 vol% and approached a saturation value at silica concentrations > 5 vol%: While the addition of 0.1 vol% silica to the YSZ samples shifted the IEP only by approximately one pH unit to pH 8.5 ± 0.3, YSZ/1 vol% silica samples and YSZ/5 vol% silica samples were characterized by IEPs in the acidic range at pH 4.7 ± 0.1 and 2.7 ± 0.2, respectively. A further increase of the silica contents to 10 or 20 vol% shifted the IEP to pH 1.5 ± 0.5 and < 1.2 ± 0.1, respectively.

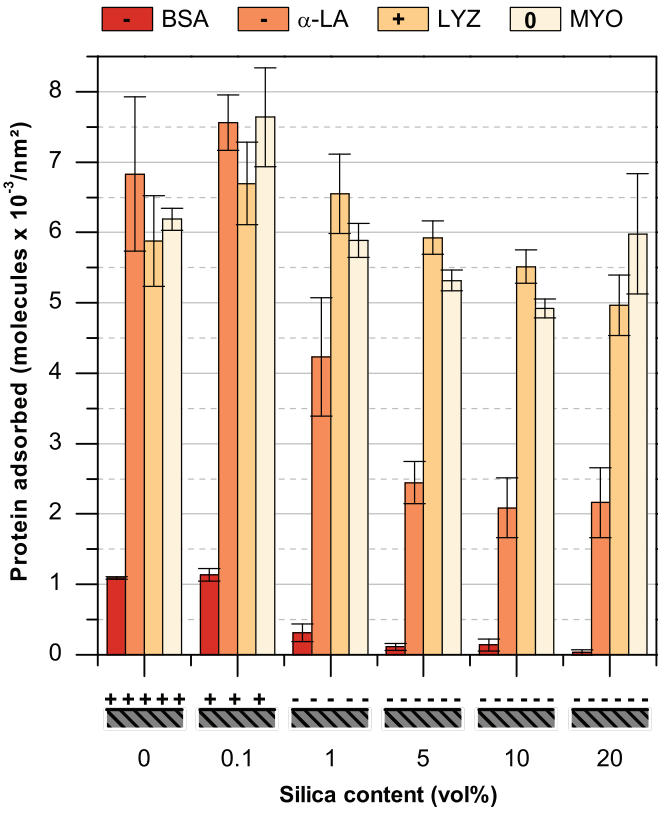

Fig. 7. Amount of adsorbed proteins (molecules × 10^{-3}/nm^2) on yttria stabilized zirconia/silica ceramics at pH 7. At pH 7, bovine serum albumin (BSA) and α-lactalbumin (α-LA) are negatively charged, lysozyme (LYZ) is positively charged and myoglobin (MYO) has an overall neutral surface potential. The zeta potential of the porous ceramic materials is schematically indicated.

To showcase the effect of the silica content in YSZ/silica ceramics on the electrostatic attachment of colloids, protein adsorption experiments have been carried out at pH 7 using proteins with different IEPs and sizes. Fig. 7 displays the results of these experiments and schematically indicates the zeta potential of the different ceramic materials at pH 7 (see also Fig. 6(A)).

A variation in the sign and magnitude of the surface charge had a large impact on the adsorption behavior of the two negatively charged proteins BSA and α-lactalbumin (α-LA), while the positively charged lysozyme (LYZ) and the neutral myoglobin (MYO) exhibited a more or less stable amount of adsorbed proteins on substrates with varying silica content. Compared to the other proteins, bovine serum albumin (BSA) was characterized by the smallest amount of surface-adsorbed proteins, expressed in molecules per unit area. Approximately 1.1 × 10^{-3} BSA molecules per nm^2 were adsorbed on positively charged YSZ samples without silica and with a silica content of 0.1 vol%. On negatively charged samples with 1 to 20 vol% of silica, the BSA amount decreased from 0.31 ± 0.13 to 0.03 ± 0.04 molecules × 10^{-3}/nm^2. A similar, though less pronounced effect was observed in the case of α-lactalbumin (α-LA) adsorption on YSZ/silica samples. The highest α-LA loading of about 7 molecules × 10^{-3}/nm^2 was found on positively charged YSZ/0 vol% and YSZ/0.1 vol% samples. Approximately 2 molecules × 10^{-3}/nm^2, i.e. one third of this maximum density, was attached to samples with a silica content of 5 to 20 vol%. The amounts of adsorbed LYZ and MYO varied in narrower ranges between 4.97 ± 0.42 and 6.69 ± 0.59 molecules × 10^{-3}/nm^2 in case of LYZ and 4.92 ± 0.13 to 7.64 ± 0.70 molecules × 10^{-3}/nm^2 in case of MYO with the maximum loading on supports with 0.1 vol% silica concentration. No significant differences in the amount of adsorbed proteins were found when comparing substrates without silica and with 20 vol% silica.

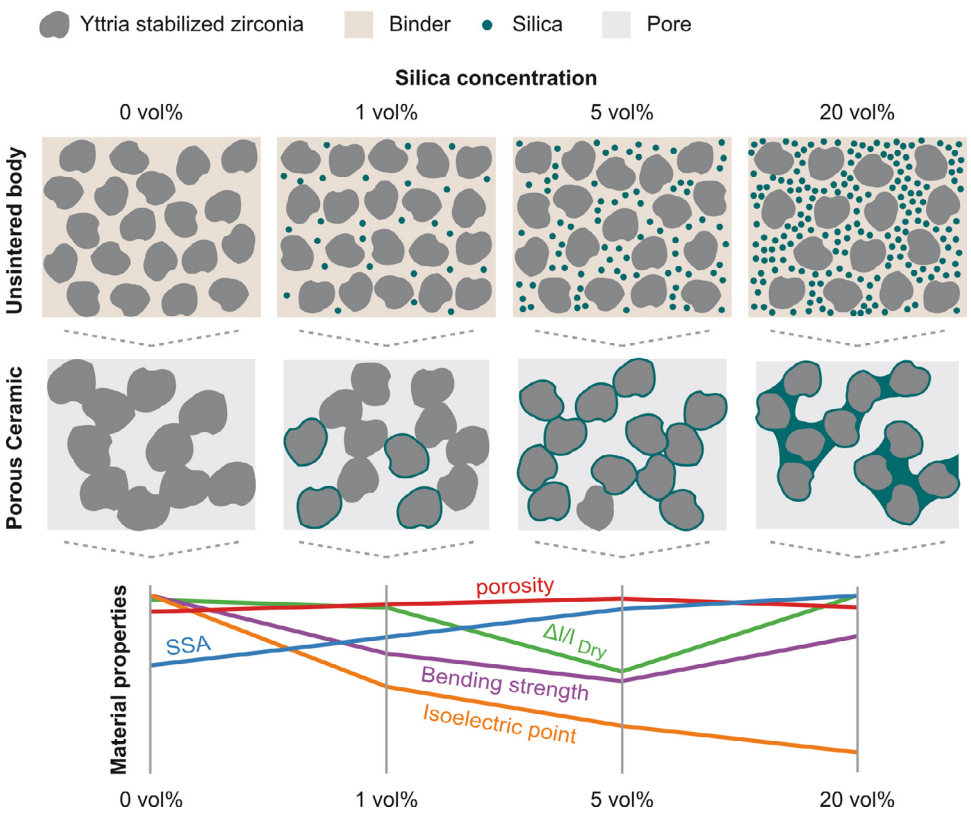

Fig. 8. Schematic of the proposed microstructure of different YSZ/silica samples prior to sintering (unsintered body) and after thermal treatment (porous ceramic) and the resulting material properties.

4. Discussion

4.1. Effect of silica addition on the microstructural evolution in porous YSZ ceramics

To effectively alter a material's electrostatic surface potential via silica-assisted sintering, the distribution of the glassy phase within the structure needs to be controlled. Therefore, the densification behavior of porous YSZ/silica ceramics, their microstructural characteristics and bending strengths were used to investigate the sintering process depending on silica addition. The effects of the silica content on the structure of the unsintered and sintered body as well as on the most important material properties are schematically summarized in Fig. 8.

The melting of silica is the precondition for the wetting of YSZ particles by the amorphous silica phase during sintering and is thus critical for the tailoring of the material's electrostatic surface potential. Microstructural images of YSZ/silica samples and their specific surface area as well as DTA analysis of the solid silica starting material suggest that the used Aerosil 300 particles melt below the maximum sintering temperature of 1050 °C. After sintering, single silica particles were not identified within the sample microstructure by SEM, instead, in samples with high silica concentrations (20 vol% silica), whole areas of amorphous silica were present (Fig. 3(H)). The unsintered silica starting powder Aerosil 300 is highly porous and characterized by a very large specific surface area of about 270 m^2/g compared to the YSZ powder (~15 m^2/g) (Table S3). The moderate specific surface area of the sintered YSZ/silica materials between 7.0 ± 0.5 and 11.7 ± 0.1 m^2/g (Table 1) indicates, that the surface area of the silica particles was drastically reduced during sintering, which would be in agreement with their melting during sintering. The slight increase in specific surface area with silica addition can be related to the inhibition of growth of the zirconia particles (Table 1, Fig. 8). In DTA, the silica starting materials underwent an overall endothermic process, which started approximately between 200 and 300 °C (Fig. S2A). This process can be interpreted as the onset of the glass transition from vitreous solid glass to a flexible plastic phase [56]. The observed low melting point of Aerosil 300 silica seems to be related to its extremely small particle size (7 nm). For quartz glass, glass transformation temperatures around 1200 °C have been reported [57].

The presence of molten silica in the samples and the resulting wetting of YSZ particles by silica gradually changed the predominant sintering mechanisms from pure solid state sintering towards liquid phase sintering [21,38,40–43,58–61]. Although the ZrO_2–SiO_2 phase diagram [62] predicts the formation of zircon ($Zr[SiO_4]$) at the sintering temperature of 1050 °C, XRD results (Fig. S7) confirm that the crystalline phase composition (monoclinic Zirconia, tetragonal YSZ, traces of zircon) remained unaffected by the silica addition. In silica-free YSZ samples, the microstructure was characterized by broad contact areas between enlarged particles (Fig. 3(C), Fig. 8) and a low sintering shrinkage of only 5.1 ± 0.4%, which is in agreement with intermediate phase solid state sintering [59–61]. The addition of silica on the other hand caused an inhibition of YSZ particle growth in YSZ/silica samples and a rounding of particles (Fig. 3(D–H), Fig. 4(A–E), Fig. 8). Amorphous particle edges in YSZ/1 vol% silica samples indicate the distribution of a very thin amorphous silica coating on the surface (Fig. 4(E)). This would be in agreement with the change in surface potential (Fig. 6). The rounding of particles at sintering necks in YSZ/1 vol% silica samples (Fig. 4(B/E)) indicates a silica accumulation at particle boundaries at least during sintering and a consequent reduction of internal stresses [21,23,24,36–38,41,45]. Particle rounding reduces the contact area between single grains, which could be a reason for the observed lower mechanical strength. The distribution of the amorphous phase on the surface further reduces the mass transport via diffusion between the solid YSZ particles with increasing glass content [27,41,50–52], due to the low solubility of zirconia in silica [45,62]. Thus, YSZ/silica samples with a concentration of up to 5 vol% silica were characterized by a decrease in sintering shrinkage, particle growth, mean pore window size and strength and an increase in porosity (Table 1,Fig. 8). At higher silica concentrations ≥ 10 vol% however, the density and strength increased compared

to YSZ/5 vol% silica samples. This indicates the densification via the liquid phase sintering processes, such as an enhanced rearrangement of zirconia particles in a liquefied silica matrix due to capillary forces [42,43,59–61]. In YSZ/20 vol% silica samples, which were characterized by the highest silica concentration, the YSZ particles appear to be rounded and partially embedded in an amorphous phase. These findings indicate an intermediate stage liquid sintering process with an almost complete wetting of the YSZ particles by silica at 1050 °C [21,23,24,35–38,41,44,45]. Consequently, the applied sintering temperature of 1050 °C was appropriate to form porous bodies by partial solid state or liquid phase sintering [58,63]. The mean pore window sizes between 71.7 ± 2.3 and 93.0 ± 0.3 nm (Table 1, Fig. 5) were however larger than expected for interparticle pores, which are characteristically 2–5 times smaller than the ceramic starting powder (10 and 30 nm), and the porosity of > 50% was quite large for a partial sintering process [64,65]. These porous properties can be attributed to the large volume of PVA binder in the unsintered body, which can act as a space holder or sacrificial template (Fig. 8). To ensure workability during the preparation of ceramic dispersion, a minor increase of the dispersant (SAD) relative to the overall particle surface area was necessary. When comparing the silica-free and the YSZ/20 vol% silica sample, the overall organic content was increased by 1.9 vol%, which could have additionally increased the porosity of the system. Since both samples do, however, not significantly differ in porosity, the influence of SAD addition on the porosity seems to be negligible. It can be noted that irrespective of the sample type, the shrinkage of the dried YSZ/samples due to debindering contributed 0.5 ± 0.2% to the overall shrinkage due to high temperature treatment.

Partial solid state and liquid phase sintering were effective in achieving a highly interconnected porous structure, that would allow for a good accessibility of the modified surface by liquids or colloidal particles for filtration or adsorption applications.

The packing of YSZ and silica particles during the drying of unsintered ceramic bodies could have also affected the oxide's behavior during sintering, the distribution of silica in the matrix as well as the resulting ceramic properties [66]. During drying of wet unsintered bodies, the samples contract due to the evaporation of water until a dry matrix is reached [66]. If permitted by the large amounts of PVA binder, the YSZ and silica particles come in contact with each other and rearrange [66]. In samples with a low amount of silica, such as 0.1 or 1 vol%, the small silica particles might have arranged in the voids between the larger YSZ powder during drying (Fig. 8). At silica concentrations between 5 and 10 vol% the voids might have been completely filled with silica particles, such that single silica particles would act as a space holders and decrease the drying shrinkage (Fig. 8). The spacing of single silica particles between YSZ particles could have given rise to amorphous film formation between YSZ particles and closed pores. Especially in 5 vol% samples, pores might have been trapped inside the silica matrix, which would have increased the overall porosity while decreasing the material's strength (Table 1, Fig. 8). At high silica levels, e.g. 20 vol%, large YSZ particles might have been embedded in a fine matrix of silica powder, which would have ensured an efficient packing in the dry state as well as a complete coating of the YSZ particles during sintering (Fig. 8).

4.2. Modification of YSZ electrostatic surface potentials using silica coatings

In the previous it has been pointed out how the microstructure of YSZ/silica ceramics is influenced by powder packing within the unconsolidated structure, by the wetting of YSZ particles with silica during the sintering process and the distribution of the silica melt by capillary forces. In the following we want to show how the IEP of YSZ/silica samples (IEP_{sample}) and thus the electrostatic surface potential can be specifically modified based on the coverage of YSZ by silica (Fig. 8).

The dependence of IEP_{sample} on the silica concentration (c_{SiO_2}) is displayed in Fig. 6(B). The experimentally derived $IEP_{sample}(c_{SiO_2})$ values were fitted successfully with an exponential decay function (Fig. 6(B), Curve Fit). The IEPs of the starting materials YSZ (IEP_{YSZ}) and silica (IEP_{SiO_2}) should serve as the boundary values to this function, with $IEP_{sample}(0)$ corresponding to IEP_{YSZ} and $IEP_{sample}(100)$ corresponding to IEP_{SiO_2}. To recreate the fitted curve (Fig. 6(B), Curve Fit) using empirically derived values, IEP_{YSZ} and IEP_{SiO_2} were approximated using the IEPs of the silica-free sample (0 vol% silica) and the sample with the maximum silica concentration (20 vol% silica), i.e. pH 9.4 and 1.2, respectively, which are in reasonable agreement with literature values [1,17,28].

Table 2
Estimated and fitting-derived parameters of $IEP_{sample}(c_{SiO_2})$ in pH units.

	IEP_{YSZ}	IEP_{SiO_2}	c_{layer}
Curve fit	9.1	1.4	1.2
Estimated	9.4	1.2	1.5

We further assume that the surface potentials of the accessible YSZ and silica surface areas contribute equally to the overall IEP of the porous material [5,16,49,67–69] and that silica forms a coating of uniform thickness (h_{layer}) on YSZ particles of uniform radius (r_{YSZ}). Therefore, if IEP_{YSZ} and IEP_{SiO_2} are known, IEP_{sample} should be dependent on the degree of silica coating on YSZ particles. This degree of coating can be expressed as the ratio of c_{SiO_2} to the minimum concentration of silica that is needed to form a complete layer on the YSZ particles (c_{layer}). With respect to the processing route, c_{layer} can indicate a change from a sintering process which is dominated by solid state sintering ($c_{SiO_2} < c_{layer}$) to the prevalence of liquid phase sintering ($c_{SiO_2} \geq c_{layer}$) with the above stated implications on the material properties. c_{layer} can be estimated using $c_{layer} = \frac{(r_{YSZ}+h_{layer})^3-(r_{YSZ})^3}{(r_{YSZ}+h_{layer})^3}\ 100$. In our experiments, $r_{YSZ} = 68.2$ nm was derived by DLS measurements and h_{layer} was approximated by the height of a single silica tetrahedron, i.e. 0.34 nm [70]. TEM measurements indicate the existence of a thin amorphous layer in that size range on the YSZ particles (Fig. 4(E)), which can most likely be attributed to the silica layer. c_{layer} was consequently calculated to be 1.5 vol% (0.6 wt%), which is in reasonable agreement with literature values [30]. Based on the previous considerations, IEP_{sample} can be described by:

$$IEP_{sample}\left(c_{SiO_2}\right) = IEP_{YSZ} * e^{\frac{-c_{SiO_2}}{c_{layer}}} + IEP_{SiO_2} * \left(e^{\frac{-c_{SiO_2}}{c_{layer}}} - 1\right) \quad (1)$$

where IEP_{YSZ} and IEP_{SiO_2} are the isoelectric points of YSZ and silica derived from streaming potential measurements and c_{layer} is the minimum silica concentration needed to form a complete layer on the YSZ particles, which is calculated based on YSZ particle radius and 0.34 nm as silica coating thickness (see above). The derived function (Estimated) is contrasted with the experimental values and the fitted curve (Curve Fit) in Fig. 6(B).

Deviations between the experimentally-derived values and the curves, especially in the case of the sample containing 5 vol% silica, could have been caused by variations in the thickness of the silica coating [16], the width of the YSZ particle size distribution and particle growth. During liquid phase sintering, the glassy phase could also have separated agglomerated particles [60], i.e. access a larger particle surface area than predicted by the DLS particle size. Slow cooling after sintering might have caused a (partial) dewetting of the YSZ particles [47], which would lead to an overestimation of c_{layer} in the curve fitting process.

The estimated and fitting-derived parameters for IEP_{YSZ}, IEP_{SiO_2} and c_{layer} (Table 2) are in very good agreement, indicating that Eq. (1) can indeed be used as a model to describe the function $IEP_{sample}(c_{SiO_2})$. We conclude that the suggested approach is appropriate to estimate the silica concentration needed for achieving a porous YSZ/silica material with a specific IEP value and to tailor the electrostatic surface potential.

4.3. Tailored adsorption capacity of YSZ/silica ceramics

The surface charge of a material can significantly affect other material properties, such as its adsorption capacity [4,16]. A systematic modification of the electrostatic surface potentials of YSZ ceramics by silica addition would thus facilitate the tailoring of the related adsorption capacity according to a specific application [16]. The process of protein adsorption is one relevant example from the fields of biocatalysis and filtration [2,3,5,18,49,71,72] and has important implications on biofouling [2,49,67,71–73]. Systematic protein adsorption experiments showed that a change in zeta potential can indeed significantly affect the material's adsorption capacity for proteins (Fig. 7). An increase in the potential difference between protein molecules and a ceramic surface generally increases the adsorption capacity of the substrate or its tendency for biofouling [50]. This trend was clearly reflected in the adsorption of negatively charged BSA and α-LA: with increasing silica content, the material's zeta potential decreased, which drastically reduced the amount of adsorbed protein. Since MYO was neutrally charged at pH 7, electrostatic interactions with the surface did not play a major role in its adsorption and the adsorbed protein amount remained almost constant with varying electrostatic surface potential of the substrate. The same trend was however observed for LYZ, which is positively charged at pH 7 and should therefore interact with a charged material surface. Due to their respective IEP values [10,54], the absolute zeta potential of LYZ at pH 7 might even be larger than the zeta potentials of BSA and α-LA. Due to the complexity of the molecular protein structure, their adsorption is however not solely controlled by electrostatic interactions, but it can be affected by their size and structure, their resistance to conformational changes and heterogeneity of surface potential and hydrophobicity on the protein surface [53]. Thus it can be speculated that the strong adsorption of positively charged LYZ to the outer surface of negatively charged porous structures could have resulted in a reversal of the surface potential, which might have prevented the molecules from entering the porous network [74]. This effect could have been more pronounced in LYZ since it is, unlike BSA, characterized as a hard protein, which usually does not undergo conformational changes such as unfolding upon adsorption to a surface [10,75]. Thus, the different types of proteins (Table S1) did not respond to variations in surface charge to the same extent.

In conclusion, the adsorption experiments of proteins have shown exemplarily how the surface potential and the adsorption capacity of porous YSZ/silica ceramics can be effectively altered due to silica-assisted sintering. The adsorption capacity of the membranes could be further tuned by a variation of the pH value during the experiment [19].

5. Conclusion

The fabrication and systematic study of porous YSZ/silica ceramics with varying silica content has shown the strong influence of silica addition on the densification behavior, sintering mechanism, on their microstructural evolution, mechanical properties and particularly electrostatic surface potential and adsorption capacity (Fig. 8). Highly porous bodies (> 50%) were formed at 1050 °C by using PVA binder as a sacrificial template and partial sintering of the YSZ skeleton. In the sintering process, a silica melt was formed which gradually changed the sintering process from solid state sintering to liquid phase sintering with increasing silica concentration (0–20 vol%). The wetting of the YSZ particles by the amorphous phase during sintering caused an inhibition of mass transport, particle growth and diffusion-induced densification as well as a rounding of particles. At high silica concentrations (≥ 10 vol%), densification due to particle rearrangements played a major role in the sintering process, which counteracted the degradation of the material's bending strength. Streaming potential measurements revealed that the IEP of YSZ ceramics can be effectively tailored by silica addition. The IEP of the YSZ/silica materials was shown to depend on the IEPs of the starting materials, the silica concentration (c_{SiO_2}) in the YSZ/silica samples and the mean particle radius of the ceramic main component (r_{YSZ}) and could be described analytically by an exponential decay function. As one relevant application example, porous YSZ/silica ceramics with tailored surface potential have been tested in protein adsorption experiments. Silica-assisted sintering has shown a great potential for the specified modification of oxide materials with respect to their zeta potential and the related adsorption capacity. Using silica-assisted sintering, stable surface modifications were achieved without the use of chemical post-processing functionalizations. This processing strategy shows great promise for the development of advanced technical oxidic materials that can be used as immobilization substrates in bioreactors, filters or biomaterials.

Declarations of Competing Interest

The authors declare that they have no competing interests.

Acknowledgments

This work was supported by the German Research Foundation (DFG), Grant No. MA 4795/13-2.

Supplementary materials

Supplementary material associated with this article can be found, in the online version, at doi:10.1016/j.mtla.2020.100735.

References

[1] M. Kosmulski, Isoelectric points and points of zero charge of metal (hydr)oxides: 50 years after Parks' review, Adv. Colloid Interface Sci. 238 (2016) 1–61.
[2] Q. Zhang, Y. Fan, N. Xu, Effect of the surface properties on filtration performance of Al_2O_3–TiO_2 composite membrane, Sep. Purif. Technol. 66 (2) (2009) 306–312.
[3] L. Ricq, A. Pierre, J.-.C. Reggiani, S. Zaragoza-Piqueras, J. Pagetti, G. Daufin, Effects of proteins on electrokinetic properties of inorganic membranes during ultra- and micro-filtration, J. Membr. Sci. 114 (1) (1996) 27–38.
[4] G.A. Parks, Aqueous surface chemistry of oxides and complex oxide minerals, in: W. Stumm (Ed.), Equilibrium Concepts in Natural Water Systems, American Chemical Society, Washington, D.C., 1967, pp. 121–160.
[5] M. Mullet, P. Fievet, J.C. Reggiani, J. Pagetti, Surface electrochemical properties of mixed oxide ceramic membranes: zeta-potential and surface charge density, J. Membr. Sci. 123 (2) (1997) 255–265.
[6] B.D. Ratner, New ideas in biomaterials science – a path to engineered biomaterials, J. Biomed. Mater. Res. 27 (7) (1993) 837–850.
[7] E. Ostuni, R.G. Chapman, R.E. Holmlin, S. Takayama, G.M. Whitesides, A Survey of structure – property relationships of surfaces that resist the adsorption of protein, Langmuir 17 (18) (2001) 5605–5620.
[8] J.A. Schwarz, C.T. Driscoll, A.K. Bhanot, The zero point of charge of silica – alumina oxide suspensions, J Colloid Interface Sci 97 (1) (1984) 55–61.
[9] M.M. Hoog Antink, T. Sewczyk, S. Kroll, P. Árki, S. Beutel, K. Rezwan, M. Maas, Proteolytic ceramic capillary membranes for the production of peptides under flow, Biochem. Eng. J. 147 (2019) 89–99.
[10] F. Meder, T. Daberkow, L. Treccani, M. Wilhelm, M. Schowalter, A. Rosenauer, L. Mädler, K. Rezwan, Protein adsorption on colloidal alumina particles functionalized with amino, carboxyl, sulfonate and phosphate groups, Acta Biomater. 8 (3) (2012) 1221–1229.
[11] J. Bartels, M.N. Souza, A. Schaper, P. Árki, S. Kroll, K. Rezwan, Amino-functionalized ceramic capillary membranes for controlled virus retention, Environ. Sci. Technol. 50 (4) (2016) 1973–1981.
[12] L. Treccani, T. Yvonne Klein, F. Meder, K. Pardun, K. Rezwan, Functionalized ceramics for biomedical, biotechnological and environmental applications, Acta Biomater. 9 (7) (2013) 7115–7150.
[13] S. Prakash, M.B. Karacor, S. Banerjee, Surface modification in microsystems and nanosystems, Surf. Sci. Rep. 64 (7) (2009) 233–254.
[14] M. Zhu, M.Z. Lerum, W. Chen, How to prepare reproducible, homogeneous, and hydrolytically stable aminosilane-derived layers on silica, Langmuir 28 (1) (2012) 416–423.
[15] V. Szczepanski, I. Vlassiouk, S. Smirnov, Stability of silane modifiers on alumina nanoporous membranes, J. Membr. Sci. 281 (1) (2006) 587–591.
[16] Y. Xu, L. Axe, Synthesis and characterization of iron oxide-coated silica and its effect on metal adsorption, J. Colloid Interface Sci. 282 (1) (2005) 11–19.
[17] M. Kosmulski, The pH dependent surface charging and points of zero charge. VI. Update, J. Colloid Interface Sci. 426 (2014) 209–212.
[18] M. Mullet, P. Fievet, A. Szymczyk, A. Foissy, J.-.C. Reggiani, J. Pagetti, A simple and accurate determination of the point of zero charge of ceramic membranes, Desalination 121 (1) (1999) 41–48.
[19] A. Mehdilo, M. Irannajad, B. Rezai, Effect of chemical composition and crystal chemistry on the zeta potential of ilmenite, Colloids Surf. A: Physicochem. Eng. Asp. 428 (2013) 111–119.

[20] A.O. Zhigachev, V.V. Rodaev, A.V. Umrikhin, Y.I. Golovin, The effect of silica content on microstructure and mechanical properties of calcia-stabilized tetragonal zirconia polycrystalline ceramic, Ceram. Int. 45 (1) (2019) 627–633.
[21] R. Ramamoorthy, R. Chaim, Microstructural evolution in nanocrystalline Y-TZP containing a silicate glass, J. Eur. Ceram. Soc. 21 (16) (2001) 2895–2902.
[22] A. Samodurova, D. Vengust, A. Kocjan, T. Kosmač, The sintering-temperature-related microstructure and phase assemblage of alumina-doped and alumina-silica-co-doped 3-mol%-yttria-stabilized tetragonal zirconia, Scr. Mater. 105 (2015) 50–53.
[23] L. Gremillard, J. Chevalier, T. Epicier, G. Fantozzi, Improving the durability of a biomedical-grade zirconia ceramic by the addition of silica, J. Am. Ceram. Soc. 85 (2) (2002) 401–407.
[24] L. Gremillard, T. Epicier, J. Chevalier, G. Fantozzi, Microstructural study of silica–doped zirconia ceramics, Acta Mater. 48 (18) (2000) 4647–4652.
[25] S.L. Hwang, I.W. Chen, Grain size control of tetragonal zirconia polycrystals using the space charge concept, J. Am. Ceram. Soc. 73 (11) (1990) 3269–3277.
[26] A. Sharif, P. Imamura, T. Mitchell, M. Mecartney, Control of grain growth using intergranular silicate phases in cubic yttria stabilized zirconia, Act Mater. 46 (11) (1998) 3863–3872.
[27] F. Del Monte, W. Larsen, J.D. Mackenzie, Chemical interactions promoting the ZrO_2 tetragonal stabilization in ZrO_2-SiO_2 binary oxides, J. Am. Ceram. Soc. 83 (6) (2000) 1506–1512.
[28] G.A. Parks, The isoelectric points of solid oxides, solid hydroxides, and aqueous hydroxo complex systems, Chem. Rev. 65 (2) (1965) 177–198.
[29] J. Werner, B. Besser, C. Brandes, S. Kroll, K. Rezwan, Production of ceramic membranes with different pore sizes for virus retention, J. Water Process Eng. 4 (2014) 201–211.
[30] T. Uchikoshi, Y. Sakka, K. Hiraga, Effect of silica doping on the electrical conductivity of 3 mol% yttria-stabilized tetragonal zirconia prepared by colloidal processing, J. Electroceram. 4 (1) (1999) 113–120.
[31] M. Gust, G. Goo, J. Wolfenstine, M.L. Mecartney, Influence of amorphous grain boundary phases on the superplastic behavior of 3-mol%-yttria-stabilized tetragonal zirconia polycrystals (3Y-TZP), J. Am. Ceram. Soc. 76 (7) (1993) 1681–1690.
[32] Y.i. Yoshizawa, T. Sakuma, Role of grain-boundary glass phase on the superplastic deformation of tetragonal zirconia polycrystal, J. Am. Ceram. Soc. 73 (10) (1990) 3069–3073.
[33] Y. Ikuhara, T. Yamamoto, A. Kuwabara, H. Yoshida, T. Sakuma, Structure and chemistry of grain boundaries in SiO_2-doped TZP, Sci. Technol. Adv. Mater. 2 (2) (2001) 411–424.
[34] R. Chaim, R. Ramamoorthy, A. Goldstein, I. Eldror, A. Gurman, Uniaxial plastic deformation in the zirconia-based nanocrystalline ceramics containing a silicate glass, J. Eur. Ceram. Soc. 23 (5) (2003) 647–657.
[35] K. Kajihara, Y. Yoshizawa, T. Sakuma, The enhancement of superplastic flow in tetragonal zirconia polycrystals with SiO_2-doping, Acta Metall. Mater. 43 (3) (1995) 1235–1242.
[36] F. Lange, H. Shubert, N. Claussen, M. Ruhle, Effects of attrition milling and post-sintering heat treatment on fabrication, microstructure and properties of transformation toughened ZrO_2, J. Mater. Sci. 21 (3) (1986) 768–774.
[37] A. Samodurova, A. Kocjan, M.V. Swain, T. Kosmač, The combined effect of alumina and silica co-doping on the ageing resistance of 3Y-TZP bioceramics, Acta Biomater. 11 (2015) 477–487.
[38] M. Mecartney, Influence of an amorphous second phase on the properties of yttria-stabilized tetragonal zirconia polycrystals (Y-TZP), J. Am. Ceram. Soc. 70 (1) (1987) 54–58.
[39] S. Deville, J. Chevalier, L. Gremillard, Atomic force microscopy study of the tetragonal to monoclinic transformation behavior of silica doped yttria-stabilized zirconia, J. Mater. Sci. 40 (14) (2005) 3821–3823.
[40] J.F. Shackelford, P. Nicholson, W. Smeltzer, Influence of SiO_2 on sintering of partially stabilized zirconia, Am. Ceram. Soc. Bull. 53 (12) (1974) 865–867.
[41] Y.J. Lin, P. Angelini, M.L. Mecartney, Microstructural and chemical influences of silicate grain-boundary phases in yttria-stabilized zirconia, J. Am. Ceram. Soc. 73 (9) (1990) 2728–2735.
[42] S. Chen, L.-.K. Liu, W. Li, Sintering behavior and dielectric properties of ultra-low temperature glass/ceramic composites, Mater. Res. Bull. 114 (2019) 107–111.
[43] D.R. Clarke, On the equilibrium thickness of intergranular glass phases in ceramic materials, J. Am. Ceram. Soc. 70 (1) (1987) 15–22.
[44] J. Zhao, Y. Ikuhara, T. Sakuma, Grain growth of silica-added zirconia annealed in the cubic/tetragonal two-phase region, J. Am. Ceram. Soc. 81 (8) (1998) 2087–2092.
[45] O. Markhsev, R. Chaim, Grain-growth kinetics in a nanocrystalline 2 yttria-stabilized tetragonal zirconia polycrystals ceramic with a silica-based glassy phase, J. Mater. Res. 18 (4) (2012) 950–955.
[46] F. Monte, W. Larsen, J.D. Mackenzie, Stabilization of tetragonal ZrO_2 in ZrO_2–SiO_2 binary oxides, J. Am. Ceram. Soc. 83 (3) (2000) 628–634.
[47] L. Gremillard, T. Epicier, J. Chevalier, G. Fantozzi, Effect of cooling rate on the location and chemistry of glassy phases in silica-doped 3Y-TZP ceramics, J. Eur. Ceram. Soc. 25 (6) (2005) 875–882.
[48] P. Thavorniti, Y. Ikuhara, T. Sakuma, Microstructural characterization of superplastic SiO_2-doped TZP with a small amount of oxide addition, J. Am. Ceram. Soc. 81 (11) (1998) 2927–2932.
[49] A. Szymczyk, P. Fievet, J.C. Reggiani, J. Pagetti, Electrokinetic characterization of mixed alumina-titania-silica MF membranes by streaming potential measurements, Desalination 115 (2) (1998) 129–134.
[50] W.R. Bowen, H. Mukhtar, Properties of microfiltration membranes: the surface electrochemistry of mixed oxide ceramic membranes, Colloids Surf. A: Physicochem. Eng. Asp. 81 (1993) 93–101.
[51] DIN Deutsches Institut für Normung e.V., Hochleistungskeramik – Monolithische Keramik; Allgemeine und Strukturelle Eigenschaften Teil 3: Bestimmung der Korngröße und der Korngrößenverteilung (Linienschnittverfahren), DIN EN 623-3, 2003.
[52] DIN Deutsches Institut für Normung e.V., Hochleistungskeramik – Mechanische Eigenschaften Monolithischer Keramik bei Raumtemperatur Teil 1: Bestimmung der Biegefestigkeit, DIN EN 843-1, 2008.
[53] S. Pasche, J. Vörös, H.J. Griesser, N.D. Spencer, M. Textor, Effects of ionic strength and surface charge on protein adsorption at PEGylated surfaces, J. Phys. Chem. B 109 (37) (2005) 17545–17552.
[54] T. Arai, W. Norde, The behavior of some model proteins at solid-liquid interfaces 1. Adsorption from single protein solutions, Colloids Surf. 51 (1990) 1–15.
[55] B.R. Ware, W.H. Flygare, Light scattering in mixtures of BSA, BSA dimers, and fibrinogen under the influence of electric fields, J. Colloid Interface Sci. 39 (3) (1972) 670–675.
[56] O. Mazurin, Problems of compatibility of the values of glass transition temperatures published in the world literature, Glass Phys. Chem. 33 (1) (2007) 22–36.
[57] K.D. Kim, G. Ondracek, Sintering and viscosity of commercial glass powders, JMSL 14 (6) (1995) 455–456.
[58] K. Matsui, Sintering kinetics at constant rates of heating: mechanism of silica-enhanced sintering of fine zirconia powder, J. Am. Ceram. Soc. 91 (8) (2008) 2534–2539.
[59] C.B. Carter, M.G. Norton, Ceramic Materials – Science and Engineering, Springer, New York, 2007.
[60] H. Salmang, H. Scholze, R. Telle, Keramik, 7th ed., Springer, Berlin, 2007.
[61] R. Riedel, I.-.W. Chen, Ceramics Science and Technology, Volume 3: Synthesis and Processing, John Wiley & Sons, Weinheim, 2011.
[62] W.C. Butterman, W.R. Foster, Zircon stability and the $Zr0_2$-$Si0_2$ phase diagram, Am. Mineral.: J. Earth Planet. Mater. 52 (5–6) (1967) 880–885.
[63] M. Lakusta, I. Danilenko, T. Konstantinova, G. Volkova, I. Nosolev, O. Gorban, S. Syniakina, V. Burkhovetskiy, The effect of a small amount SiO_2 on sintering kinetics of tetragonal zirconia nanopowders, Nanoscale Res. Lett. 12 (1) (2017) 398.
[64] A.R. Studart, U.T. Gonzenbach, E. Tervoort, L.J. Gauckler, Processing routes to macroporous ceramics: a review, J. Am. Ceram. Soc. 89 (6) (2006) 1771–1789.
[65] T. Ohji, M. Fukushima, Macro-porous ceramics: processing and properties, Int. Mater. Rev. 57 (2) (2012) 115–131.
[66] R. Ford, Ceramics Drying, Pergamon Press, Oxford, 1986.
[67] M. Nyström, A. Pihlajamäki, N. Ehsani, Characterization of ultrafiltration membranes by simultaneous streaming potential and flux measurements, J. Membr. Sci. 87 (3) (1994) 245–256.
[68] D.N. Furlong, P.A. Freeman, A.C.M. Lau, The adsorption of soluble silica at solid-aqueous solution interfaces: I. Leaching from glass – an electrokinetic study, J. Colloid Interface Sci. 80 (1) (1981) 20–31.
[69] J.P. Reymond, F. Kolenda, Estimation of the point of zero charge of simple and mixed oxides by mass titration, Powder Technol. 103 (1) (1999) 30–36.
[70] F. Liebau, Structural Chemistry of Silicates: Structure, Bonding, and Classification, Springer Science & Business Media, Berlin, 1985.
[71] R.S. Faibish, Y. Cohen, Fouling-resistant ceramic-supported polymer membranes for ultrafiltration of oil-in-water microemulsions, J. Membr. Sci. 185 (2) (2001) 129–143.
[72] T. Moritz, S. Benfer, P. Árki, G. Tomandl, Influence of the surface charge on the permeate flux in the dead-end filtration with ceramic membranes, Sep. Purif. Technol. 25 (1) (2001) 501–508.
[73] X. Shi, G. Tal, N.P. Hankins, V. Gitis, Fouling and cleaning of ultrafiltration membranes: a review, J. Water Process Eng. 1 (2014) 121–138.
[74] J.A. Brant, U. Igwe, Aggregation and fouling impacts in determining organic and clay removal by electropositive filtration, J. Environ. Eng. 143 (9) (2017) 04017064.
[75] M. Lepoitevin, M. Jaber, R. Guégan, J.-.M. Janot, P. Dejardin, F. Henn, S. Balme, BSA and lysozyme adsorption on homoionic montmorillonite: influence of the interlayer cation, Appl. Clay Sci. 95 (2014) 396–402.